Applied Acoustics 224 (2024) 110144



Contents lists available at ScienceDirect

Applied Acoustics

journal homepage: www.elsevier.com/locate/apacoust



Monitoring holograms for therapeutic ultrasound using passive cavitation beamforming

Nathalie Lamothe [a], Diana Andrés [a], Alicia Carrión [a], Francisco Camarena [a], José A. Pineda-Pardo [b], Noé Jiménez [a,*]

[a] Instituto de Instrumentación para Imagen Molecular (i3M), Universitat Politècnica de València, Consejo Superior de Investigaciones Científicas (CSIC), Camino de Vera S/N, València, 46011, Spain
[b] HM CINAC (Centro Integral de Neurociencias Abarca Campal), Hospital Universitario HM Puerta del Sur, HM Hospitales, Madrid, 28938, Spain

ARTICLE INFO

Keywords:
Acoustic holograms
Passive beamforming
Therapeutic ultrasound
Passive cavitation detector

ABSTRACT

Acoustic holograms can generate cavitation patterns of complex spatial distribution by shaping and steering the focal spot of therapeutic ultrasound systems. However, when monitoring these systems by passive cavitation detection, off-axis therapeutical targets and the receiver directivity may not be aligned. In this paper, we present passive cavitation beamforming to monitor a therapeutical ultrasound system using holograms targeted to arbitrary locations, in which both therapeutic and passive cavitation monitoring systems use 3D-printed acoustic lenses. The therapeutic system uses an acoustic hologram to focus the ultrasound beam on the target, which is off-axis. Then, a second lens is designed to beamform the cavitation signals which emerge from the therapeutic target, steering the directivity of the passive cavitation detector in the direction of the therapeutic focus and, in addition, compensating for skull aberrations. The system is experimentally tested with an ex-vivo macaque skull and a blood vessel phantom with microbubbles. In addition, results are compared with a standard confocal configuration and an off-axis configuration in the absence of the monitor lens. A parametric study is performed by varying the amplitude of the emitted signal and the impact on the behaviour of the microbubbles is analysed based on the cavitation index values. Results show that monitoring holograms align the passive cavitation detector response with the focal spot of the targeted therapeutic transducer. These holograms encode a fixed beamformer for cavitation signals in reception, increasing the sensitivity of cavitation emission at the target. In this way, cavitation doses can be used to locally monitor the cavitation activity of microbubbles, thus opening a new path to low-cost monitoring of therapeutic ultrasound systems.

1. Introduction

In the central nervous system (CNS), brain vasculature presents particular physiological structure, known as the blood-brain barrier (BBB), which prevents many macromolecules from entering the brain through normal paracellular or diffusion pathways. In the brain, endothelial cells composing the blood vessels and capillaries are connected by tight junctions that protects the brain by limiting the entry of potentially neurotoxic plasma components, blood cells, and pathogens [1]. However, this extremely low permeability also blocks the pathway of most potentially effective therapeutic agents or contrast molecules used for diagnostics [2]. Focused ultrasound in combination with microbubbles is nowadays the only approach to produce a transient, non-invasive, safe and localized BBB opening, thus facilitating targeted drug delivery to the brain [3].

Numerous preclinical studies have shown successful results in Alzheimer's disease (AD) treatment by using gene therapy [4,5] and antibody delivery [6], as well as in Parkinson's disease (PD) treatment by targeting pathogenic factors [7] or by delivering therapeutic agents [8,9], and glioblastoma by facilitating transfer of chemotherapeutic and other agents to improve tumour control rates and animal survival [10]. More recently, clinical trials have shown the safety and effectivenesses of focused ultrasound-induced BBB opening, e.g., for brain metastases treatment [11] and feasibility, or safety and reversibility of BBB opening in patients with AD [12,13] and PD [14].

A physical limitation of ultrasonic BBB opening techniques is the presence of the skull. Indeed, these rigid and porous bones produce

* Corresponding author.
E-mail address: nojigon@upv.es (N. Jiménez).

https://doi.org/10.1016/j.apacoust.2024.110144
Received 8 February 2024; Received in revised form 21 May 2024; Accepted 17 June 2024
0003-682X/© 2024 The Author(s). Published by Elsevier Ltd. This is an open access article under the CC BY license (http://creativecommons.org/licenses/by/4.0/).

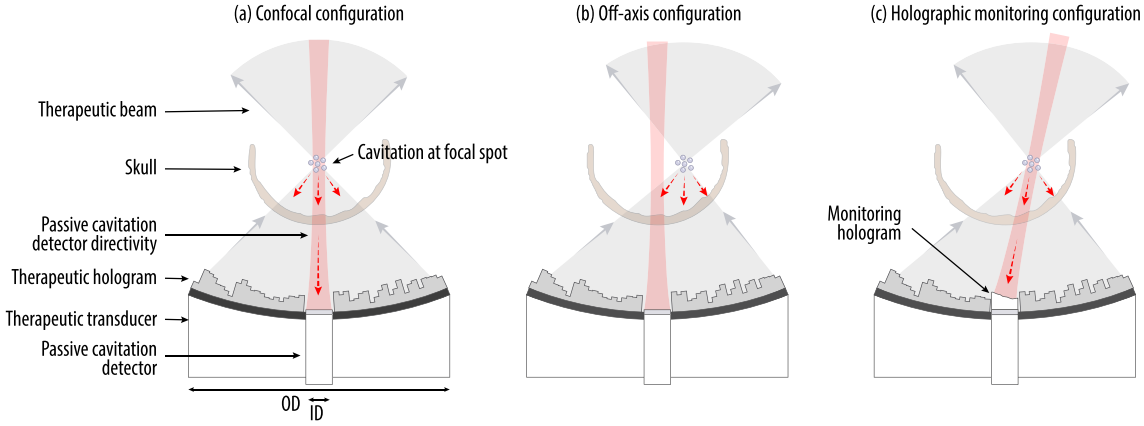


Fig. 1. Configurations used. (a) Confocal configuration where the therapeutic focus (i.e., the acoustic image) is aligned with the passive cavitation detector (PCD) directivity. (b) When the acoustic image is steered to target off-axis locations, the PCD directivity may not be aligned. (c) Using a monitoring hologram, the PCD directivity is re-aligned with the acoustic image.

aberrations and a strong attenuation of the incident ultrasound beam. Single element devices can be used to focus ultrasound in the brain, and since aberration cannot be corrected, simulations can be used to select the best-case scenario [15]. A way to get rid of skull limitations is the use of implantable ultrasound devices [16,17]. Even while this solution is evidently invasive, it may be appropriate to deliver chemotherapeutic agents after open brain surgery. Currently, the main non-invasive approach is the use of phased-array transducer systems [18,19], that allows electronic beam steering and aberration correction. However, these systems present some limitations. First, the poor scalability of the power electronics for these multiple-channel systems results in a high-cost device with a limited number of channels, only 1024 or 2048 piezoelectric emitters are commonly used. Moreover, large apertures are required to achieve a high acoustic gain. As a consequence of the combination of these two limitations, the individual piezoelectric elements must be large to cover the entire transducer aperture. Therefore, each element radiates a highly directional beam, and their centre-to-centre spacing is larger than one wavelength. This results in the emergence of diffraction grating lobes, which considerably limits the steering range of the array.

Recently, three-dimensional printed acoustic lenses were proposed to correct skull aberrations and focus ultrasound in a single spot [20]. The advantage of this system is its low-cost. It only requires a single-element transducer coupled to a 3D-printed lens. Moreover, acoustic holograms [21] can go beyond these lenses and, in addition to compensating skull aberrations, they can synthesize arbitrary wavefronts. This includes arbitrary beam steering, generating multiple focal spots, or producing complex acoustic images matching the 3D-shape of a target brain structure [22]. Since then, holograms have widely been used in many applications, such as in synthesizing acoustic vortices into the skull [23], cavitation pattern generation [24], cell patterning [25], producing arbitrary and large thermal patterns [26], controlling the thermal dose of high-intensity focused sources [27], and have been tested in vivo to open the blood-brain barrier in small animals, generating either multiple sharp focal spots whose small spherical size approaches the limit imposed by diffraction [28] or wide and elongated focal areas [29].

Even when ultrasound focusing can be efficiently achieved using holograms, the problem of monitoring the treatment is still an open issue. Since one of the most robust indicators of BBB opening is the acoustic emission produced by the cavitation of microbubbles [30,31], spectral algorithms have been developed for the detection of sub-harmonic, harmonics and ultra-harmonics generated by cavitation activity [32–34]. Quantitative indexes can be calculated to evaluate the cavitation dose [35]. Moreover, these indexes are used to implement acoustic feedback systems to dynamically control the power delivery system and limit in real time the dose delivered [36–38]. Usually, BBB monitoring systems use one or several passive cavitation detectors (PCD) to listen to the acoustic emission at the focal spot of the system. In conventional systems, the PCD is usually confocal to the focused ultrasound transducer because the detector directivity must be aligned with the therapeutic focal spot. However, when a hologram is used to generate an acoustic image which is not aligned with the axis of the holographic system or, alternatively, when certain levels of electronic steering are employed in a phased-array system, e.g., when focusing at some lateral structure in the brain, the therapeutic focal spot may not be aligned with the PCD reception directivity. This misalignment may result in a reduced cavitation signal level and the loss of calibration when comparing cavitation indexes for different targets. In this situation, cavitation mapping methods can image bubble activity and steer the detector directivity [39–43], but this method requires a high-cost phase-array system which may limit the 3D-printed lens benefits. In this way, it would be desirable to conceive a low-cost technique to steer the detector directivity to match the location of the acoustic images generated by holograms.

In this work, we present a passive cavitation detection system designed to monitor ultrasound-assisted BBB opening using holograms targeting at arbitrary locations, in which both therapeutic and monitoring systems use 3D-printed acoustic lenses. First, the therapeutic system makes use of an acoustic hologram to focus the ultrasound beam at the target, which is located off-axis. Then, a second lens is designed to steer the directivity of the PCD in the direction of the therapeutic focus and, in addition, compensating the skull aberrations. This monitoring hologram encodes a passive beamformer that amplifies the signals generated at the target, with the aim of locally monitor the cavitation activity. The system is experimentally tested using an ex-vivo macaque skull and a blood-vessel phantom including microbubbles. In addition, results are compared with a confocal configuration, as shown in Fig. 1 (a), and an off-axis configuration in the absence of the monitoring lens, as shown in Fig. 1 (b). The experimental setup consists of a dual transducer system, a passive cavitation detector and a 0.5-MHz focused ultrasound transducer coupled with a holographic lens. Blood vessels are mimicked by a 0.9-mm polyethylene flexible tube with flowing microbubbles. A parametric study is conducted by varying the amplitude of the emitted signal and microbubble activity is analysed based on cavitation index values.

2. Methods

2.1. Hologram design

The acoustic focal spot of the focused transducer is steered by using holograms, placed in contact with the surface of the transducer by using

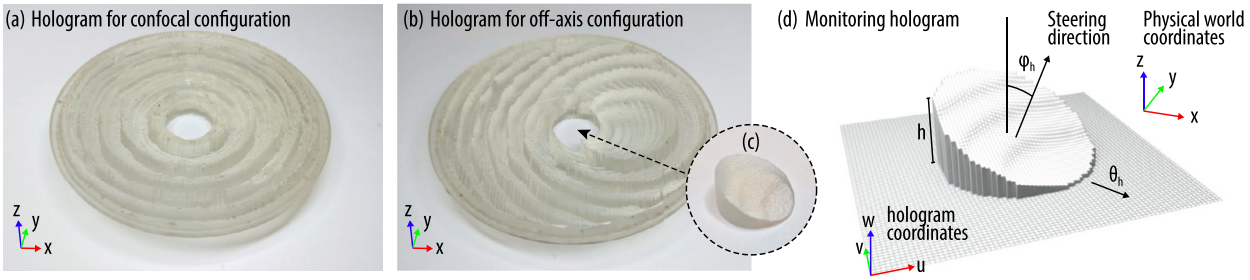


Fig. 2. Photographs of the holographic lenses for the therapeutic beam (a) confocal configuration, (b) off-axis configuration, (c) photograph of the monitoring hologram for the passive cavitation detector, (d) design scheme for the monitoring hologram.

coupling gel. In this work, two different lenses are used to tune the therapeutic beam, a confocal and an off-axis lens, and a third hologram is used for the monitoring system.

For the confocal case, Fig. 1 (a), a hologram is used to correct skull aberrations and focus at an axial distance of $z = 55.3$ mm without lateral steering. Then, for the off-axis case, Fig. 1 (b), a second hologram is used to focus on a target of interest inside the macaque skull, matching the postcomissural putamen location, whose centre is located at coordinates $x = -6.6$ mm, $y = -11.2$ mm, and at the same axial distance. Both lenses were designed using time-reversal methods using pseudo-spectral time-domain simulations, as described in detail in Ref. [21]. First, a simulation is set by locating an acoustic monopole source, namely the virtual source, at the target location inside the skull. The simulation is performed and we record the field at a spherical holographic surface parallel to the transducer, at a distance $r_0 = 4$ mm from its surface. Note in this simulation the transducer is not used as a source. Second, only the phase information of the wavefront at steady state and at the working frequency is retained, and it is complex-conjugated to account for temporal inversion. Finally, the lens is constructed to modulate the field radiated by the focused ultrasound transducer, in such a way the phase of the transmitted field by the lens resembles the phase of the wavefront at the holographic surface. The design of the lens in curvilinear coordinates is described by D. Andrés et al. [22, Supplementary material], and the macaque skull properties are described by D. Andrés et al. [44].

The monitoring hologram for the passive cavitation detector, Fig. 1 (c), was designed in the same way as the holographic lens for lateral focusing, but in this case the field was recorded at a flat surface in front of the PCD at $z_0 = 4$ mm. The complex-conjugated phase was 2D unwrapped [45], to avoid phase jumps and improve directivity in a broadband spectrum. Using the unwrapped phase, the monitoring lens was designed as those for transmission [21].

The 3D-printed lenses used are shown in Fig. 2 (a-c). All lenses were 3D printed with Clear (Formlabs) photopolymer using stereolithography (Form2, Formlabs). The lenses were designed using a pixel size of 500 μm and printed using lateral spatial resolution of 10 μm (u-v directions) and an axial resolution of 50 μm (w direction, see Fig. 2 (d)). The density and sound speed values were experimentally obtained ($\rho_L = 1186$ kg/m^3 and $c_L = 2599$ m/s, respectively), and the attenuation coefficient in the simulations was set to $\alpha_L = 3.4$ dB/(cm-MHz$^\gamma$), with a power law exponent of $\gamma = 1.1$ [44].

2.2. Hardware design

A custom piezoelectric focused ultrasound transducer is used for the therapeutic beam (single-element, 100-mm aperture, 140-mm curvature radius, 20-mm diameter of the central hole, and a central frequency of $f_c = 500$ kHz). A piezoelectric PCD (V382-SU, Olympus) with a centre frequency of 3.5 MHz and a bandwidth (− 6 dB) of 65.17%, and an aperture of 12.7 mm is used to capture the signal emitted by microbubbles cavitation. The PCD is placed in the central hole of the focused transducer in a way that both transducers are confocally aligned. The PCD acoustic focus is located at 48 mm, and its depth of field is 27 mm. A USB oscilloscope with integrated function generator (Handyscope HS5, TiePie engineering) is used for both, acquisition and signal generation. The emitted signal is amplified by a 400 Watts amplifier (E&I Ltd, USA) and a 50-Ohm impedance matching network is used to maximize power transfer from the amplifier to the focused transducer.

2.3. Experimental protocol

The dual transducer setup was submerged in a water tank filled with degassed water at room temperature. For the three experimental configurations, as shown in Fig. 1, the lenses were coupled to the transducer with high-temperature coupling gel (Sonotech Sono 600) to avoid its dissolution in water ensuring a smooth coupling of the lens to the transducer surface.

The macaque skull was located at the design position by using a 3D-printed holder, guaranteeing an accurate alignment between the skull and the holographic lens. The skull bones were submerged in degassed water during 12 hours before the experiment to avoid air pockets on its surface. Vessel phantom was manufactured using a 0.9-mm diameter polyethylene flexible tube, located in the focal zone. The precise 3D positioning was performed by using a hydrophone (Y-104, Sonic Concept), attached to a threaded rod and monitored by a motion controller (PI Micos GmbH, Germany). Then, the hydrophone was removed and replaced by the vessel phantom. Two different configurations of the vessel phantom were tested (see Fig. 3). First, a 3D-printed holder was used to stretch the tube and, thus, resulting in a straight tube transversally passing through the focal point. The second configuration consisted in performing a knot with the polyethylene tube to mimic a more complex network of the phantom vessels. Because the straight tube is a straightforward and repeatable arrangement, it requires a high precision during positioning to ensure that the 0.9-mm diameter tube overlaps the focal spot. In contrast, the knot covers a larger area, around $10 \times 10 \times 20$ mm^3. Note the size of the focal spot was $5 \times 4 \times 14$ mm^3. Therefore, knot phantom may be less sensible to positioning errors.

We used sinusoidal pulsed bursts of 100 ms length (5000 cycles), repeated at a pulse repetition frequency (PRF) of 1 Hz, during 100 s ($M = 100$ pulses). These signals feed the 0.5-MHz focused ultrasound transducer at different input voltages, which before amplification ranged from 100 mV to 600 mV, with a 100-mV step. A calibration of the system was performed to measure the peak rarefaction pressure at the focal point.

For each sinusoidal pulsed burst emitted by the therapeutic transducer, a synchronous acquisition was performed to record the cavitation signals detected by the PCD using a 100 MHz sampling frequency. Before microbubble injection, with only PBS circulating through the polyethylene tube, cavitation baseline signals were measured as a reference. Then, microbubbles (Luminity, Lantheus Medical Imaging) diluted in 5 mL of phosphate buffered saline (PBS) (final concentration of 20 μL/kg) were injected by using an infusion pump (Perfusor fm, B Braun) at a flow rate in the tube of 0.02 mL/s. Experiments were re-

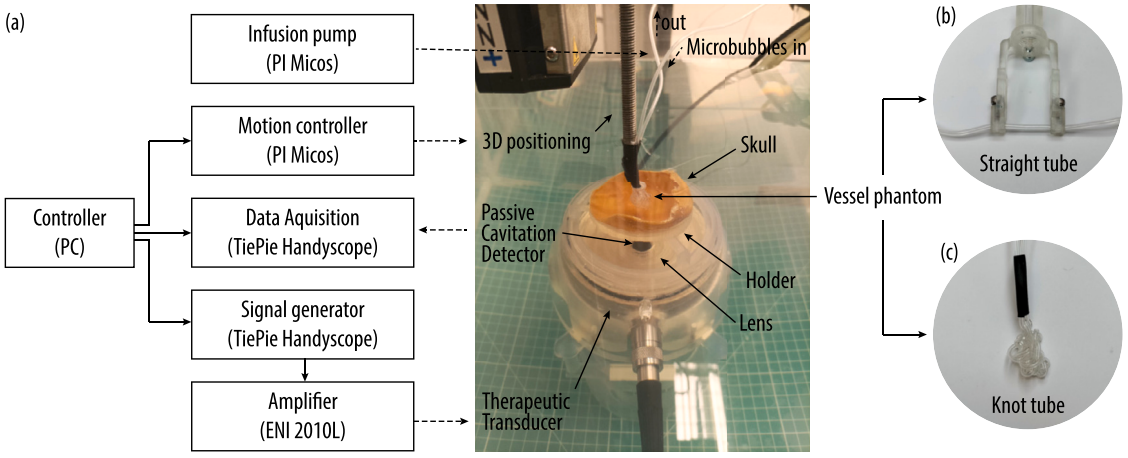


Fig. 3. (a) Block diagram for the experimental setup, photograph of the experiment, and details of the vessel phantoms: (b) straight and (c) knot tube.

peated for each phantom using the confocal configuration, and for the three configurations using the knot phantom.

2.4. System calibration

System calibration to know the input voltage versus the pressure at the focal point was performed. A high intensity hydrophone (Y-104, Sonic Concepts) was used to measure the field for the two therapeutic beam lenses in a degassed water tank, including the macaque skull but in the absence of the vessel phantom. To find the position of the focal point, 3D-scans were carried out around the coordinates of the focal spot. Final positioning of the hydrophone corresponds to the maximum pressure point. Input voltage for calibration was fixed within the range 50 mV to 700 mV, using steps of 50 mV.

In addition, the directivity of the monitoring hologram was evaluated using pseudo-spectral time-domain simulations implemented in the k-Wave package [46] and experimental measurements. The field of the PCD with and without the monitoring lens was measured in a square transverse plane of 20×20 mm^2 using a step of 0.1 mm, using a broadband hydrophone (HGL500, Onda, UK) in a degassed water tank. Then the radiation of the piezoelectric PCD was evaluated both in the near and in the far field using angular spectrum projection [44]. In the near field, experimental measurements were used to estimate the field radiated by the PCD in an area covering the focal spot. In the far field, the angular spectrum and the directivity in the elevation plane of the source were calculated. For the angular spectrum the energy of the wave is obtained for each wavevector component. Defining θ and φ as the azimuth and elevation angles in the range $0 \le \theta < 2\pi$, and $0 \le \varphi \le \pi$, the wavevector components are given by $k_x = k\cos(\theta)\sin(\varphi)$, $k_y = k\sin(\theta)\sin(\varphi)$, and $k_z = k\cos(\varphi)$, and the wavenumber is given by $k^2 = k_x^2 + k_y^2 + k_z^2 = \omega^2/c_0^2$. In this way, the far field pressure $|p|^2(k_x, k_y)$ shows the angular distribution of the acoustic wavefront energy emitted by a transducer. Note that piezoelectric PCDs are reciprocal transducers, so emission and reception responses are analogous.

2.5. Cavitation dose model

Time-domain cavitation signals, $S(t)$, were acquired and spectral processing was performed by calculating their Fast Fourier Transform, $S(f) = \mathcal{F}[S(t)]$. Several cavitation dose indexes were calculated: first, stable cavitation dose based on harmonics contribution (dSCD$_h$), second, stable cavitation dose based on ultra-harmonics contribution (dSCD$_u$) and, third, inertial cavitation dose (dICD). On the one hand, harmonic components were defined as integer multiples of the fundamental frequency,

$$f_{h,n} = nf_0, \tag{1}$$

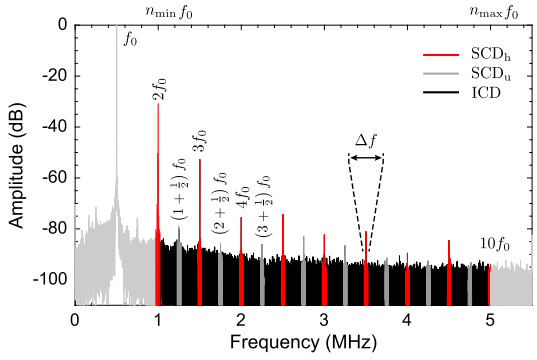


Fig. 4. Sample spectrum of the received signal. Frequency bands used for cavitation dose index are marked in colour.

where $n \in \mathbb{N}$, and $n_{\min} < n < n_{\max}$. On the other hand, ultra-harmonics were defined as odd multiples of the fundamental,

$$f_{u,n} = (n - 1/2)f_0. \tag{2}$$

A bandwidth of Δf around each harmonic or ultra-harmonic component is considered. Finally, inertial cavitation level was defined as the broadband noise contribution of the whole spectrum removing the frequency range and bandwidth of both, harmonics and ultra-harmonics,

$$(f_{h,n} + \Delta f/2) < f_{b,n} < (f_{u,n} - \Delta f/2), \text{ and}$$
$$(f_{u,n} + \Delta f/2) < f_{b,n} < (f_{h,n+1} - \Delta f/2). \tag{3}$$

These frequency bands are sketched in Fig. 4 for a sample cavitation spectrum.

For each single pulse, stable cavitation level based on harmonic contribution was defined as

$$\text{SCD}_h = \sqrt{\sum_{n=n_{\min}}^{n_{\max}} \left\langle S(f_{h,n}) \right\rangle^2}, \tag{4}$$

where $S\langle f_{h,n}\rangle$ is the area under the frequency spectrum for the n-th harmonic given by Eq. (1), considering a bandwidth of Δf around each harmonic. The stable cavitation level based on ultraharmonic components, $f_{u,n}$, is given by

$$\text{SCD}_u = \sqrt{\sum_{n=n_{\min}}^{n_{\max}} \left\langle S(f_{u,n}) \right\rangle^2}, \tag{5}$$

where $S\langle f_{u,n}\rangle$ corresponds to the area under the frequency spectrum for the n-th ultra-harmonic component given by Eq. (2), also considering a Δf bandwidth. Finally, inertial cavitation level was calculated as

$$\mathrm{ICD} = \sqrt{\sum_{n=n_{\min}}^{n_{\max}} \left\langle S(f_{b,n}) \right\rangle^2}, \tag{6}$$

where $S\langle f_{b,n}\rangle$ corresponds to the area under the broadband frequency spectrum given by Eq. (3).

Mean cavitation doses are then calculated as the mean of cavitation levels for all pulses. For the mean stable cavitation dose based on harmonics contribution we get

$$\mathrm{dSCD}_h = \frac{1}{M}\sum_{m=1}^{M} \mathrm{SCD}_{h,m}, \tag{7}$$

where $\mathrm{SCD}_{h,m}$ is the stable cavitation level based on harmonic contribution, Eq. (4), $m = 1, 2, \ldots, M$ is the pulse index and M is the total number of pulses. The mean stable cavitation dose based on ultra-harmonics contribution is given by

$$\mathrm{dSCD}_u = \frac{1}{M}\sum_{m=1}^{M} \mathrm{SCD}_{u,m}, \tag{8}$$

where $\mathrm{SCD}_{u,m}$ is the stable cavitation level based on ultra-harmonic contribution, Eq. (5). Finally, the mean inertial cavitation dose

$$\mathrm{dICD} = \frac{1}{M}\sum_{m=1}^{M} \mathrm{ICD}_m, \tag{9}$$

where ICD_m is the stable cavitation level based on harmonic contribution for the m-th pulse.

Those indexes are measured first in the absence of microbubbles to estimate a baseline level, and then injecting the microbubbles to calculate the actual cavitation doses. In this way, we can normalize the mean cavitation doses by the mean baseline (BL) dose as

$$\langle \mathrm{dSCD}_h \rangle = (\mathrm{dSCD}_h - \mathrm{dSCD}_{\mathrm{h,BL}})/\mathrm{dSCD}_{\mathrm{h,BL}}, \tag{10}$$

$$\langle \mathrm{dSCD}_u \rangle = (\mathrm{dSCD}_u - \mathrm{dSCD}_{\mathrm{u,BL}})/\mathrm{dSCD}_{\mathrm{u,BL}}, \tag{11}$$

$$\langle \mathrm{dICD} \rangle = (\mathrm{dICD} - \mathrm{dICD}_{\mathrm{BL}})/\mathrm{dICD}_{\mathrm{BL}}. \tag{12}$$

In this way, normalized doses estimate the harmonic contribution of the emission of the microbubbles in the phantom, neglecting other external sources of nonlinearity such as the nonlinear response of the materials, transducer, and cumulative nonlinear effects, or local nonlinearities such as clapping between boundaries or oscillations of solitary bubbles. In this study, it was considered a bandwidth of $\Delta f = 20$ kHz, $n_{\min} = 2$ and $n_{\max} = 10$, matching the frequency range of the PCD.

2.6. Cavitation dose dynamical model

To model the evolution of the cavitation doses we use a simple and empirical model, aiming to capture the main macroscopic features of this complex dynamical process. In this way, cavitation dose indexes were fitted to a sigmoid function, using a logistic curve given by

$$D(p) = \frac{D_{\max}}{1 + e^{-\beta(p - p_{th})}} + D_0, \tag{13}$$

where $D(p)$ is either normalized cavitation dose index, i.e., those given by Eqs. (10)-(12), as a function of the rarefaction pressure amplitude p, and the model parameter $D_{\max}$ is the maximum cavitation dose index, β is the transition scale factor, p_{th} is the cavitation pressure threshold, and D_0 is the cavitation dose baseline.

This empirical model, sketched in Fig. 5, describes the expected rise of the cavitation indexes as a function of the pressure amplitude and the transition towards the cavitation index saturation, the latter produced when energy is transferred to novel frequency components due to nonlinear cascade processes. In this way, we set the hypothesis that the model threshold value, p_{th}, for the $\mathrm{SCD_h}$ may be used to estimate the pressure threshold for stable cavitation regime. We chose this model also for inertial cavitation dose because this index must be bounded. When energy is pumped by the fundamental frequency component, the nonlinear oscillations of cavitating bubbles generate acoustic emissions with harmonic and ultra-harmonic components. As the amplitude of the pumping wave rises, so is the richness of the spectral combinations, containing harmonics, sub-harmonics and, progressively, any linear combinations of the spectral components. Therefore, the spectrum broadens, and inertial cavitation dose progressively grows. However, as the bandwidth of the PCD is finite, and absorption is more effective on higher harmonic components, we expect inertial cavitation dose to saturate. Nevertheless, note that the range of amplitudes explored in this paper are moderate and inertial cavitation dose will be restricted to its initial rise, as depicted in Fig. 5.

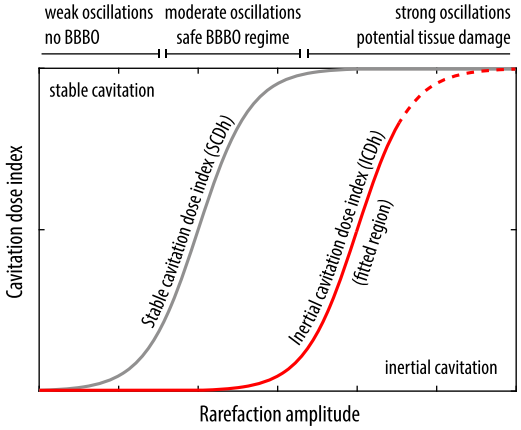


Fig. 5. Empirical cavitation model using a sigmoid function to separate stable and inertial cavitation regimes.

3. Results

3.1. Therapeutic beam calibration

The field of the therapeutic beam generated by the two lenses is presented in Fig. 6. First, for the confocal configuration we can observe that the therapeutic holographic lens is manipulating the phase of the wavefront in such a way that a sharp focal spot is generated at the axis of the system and inside the skull cap, as shown in Fig. 6 (a). The inset shows the comparison between the simulated and experimental fields, where a good agreement can be observed. Then, the second holographic lens is used to steer the focal spot towards the therapeutic target. The corresponding simulated field is shown in Fig. 6 (b), where it can be observed that the focal spot matches the location of the target. The experimental results, shown in the inset, also present a good agreement with the simulated field distribution.

Once the focal spot is identified, hydrophone measurements were taken at different driving voltages. The results of the amplitude calibration are presented in Fig. 7 for the two holograms, i.e., the confocal lens and off-axis lens, where the peak rarefaction pressure is plotted versus the input voltage. Results show that when input voltage increases, the pressure at the focal spot also increases, but the particular ratio between the applied voltage versus the peak rarefaction pressure is different for each configuration. The confocal configuration curve (red line in Fig. 7) presents a steeper slope than the off-axis calibration curve (grey curve). This means that for the same input voltage, confocal lens allows reaching a higher rarefaction pressure amplitude. For example, to reach the reference value of 0.5 MPa at the focal point, an input voltage of 240 mV is needed in the confocal configuration whereas 300 mV

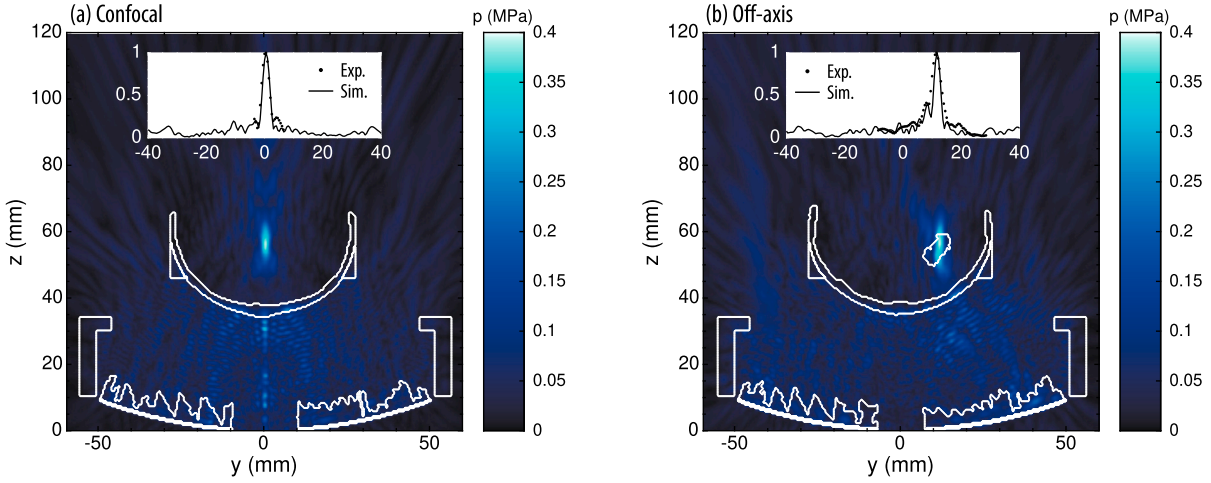


Fig. 6. Therapeutic beam field distribution. (a) Simulated field of the confocal configuration. The inset shows the experimental and simulated data for a cross-section at the focal position. (b) Off-axis configuration. The inset shows the corresponding experimental and simulated data.

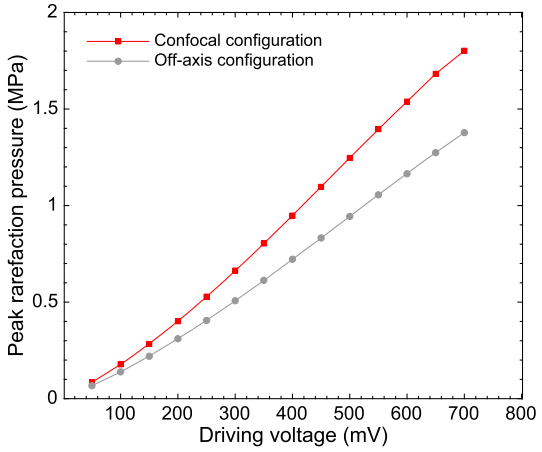


Fig. 7. Experimental calibration curves of the pressure in the focal zone versus the input voltage for confocal (red) and off-axis (grey) configurations.

are needed in the off-axis configuration, which is a 25% higher voltage. In this way, steering the focal spot leads to a reduction of the gain of the system.

Calibration results will be applied thereafter to show comparable results of the microbubbles cavitation depending on the experimental configuration. In this way, measurements acquired using amplitudes between 100 mV and 600 mV correspond to a pressure range of 178 kPa to 1.54 MPa for the confocal configuration and a range of 139 kPa to 1.16 MPa for off-axis configuration.

3.2. Monitoring hologram response

The monitoring hologram response is evaluated by projecting the field measurements using acoustic holography. Fig. 8 summarizes the main results. First, experimental results show that in the absence of the monitoring lens, the PCD shows near-field oscillations, with a final maximum at its Fresnel distance given by $z = ka^2/2\pi = 94.1$ mm, as shown in Fig. 8 (a). The PCD presents a narrow beamwidth, and, therefore, a sharp angular spectrum, see Fig. 8 (b). The beam width is $\varphi_{BW} = 1.98°$, matching the theoretical value of a circular piston for narrow beams $\varphi_{BW} = 3.232/ka = 1.99°$, where a is the radius of the source and k the wave number. Note that in the experiment the surface velocity is usually lower at the edges and the approximation of a uniform circular piston is not exactly fulfilled. Nevertheless, as shown in Fig. 8 (c), the PCD agrees with the theoretical response of a flat circular radiator given by $p(\varphi) = 2J_1(ka\sin\varphi)/ka\sin\varphi$, where J_1 is the first-order Bessel function of the first kind.

It is important to note that if a cavitation source is located out of axis, for example, at elevation angles larger than 10°, like those in the off-axis configuration, Fig. 1 (b), then the detected cavitation signal amplitude falls to less than 20 dB, i.e., signals are attenuated by two orders of magnitude. In this situation, cavitation noise generated out of the target might mask the cavitation signals of interest generated at the target region.

In contrast, when the monitoring hologram is used, we observe that the PCD beam in transmission is steered and refocused to the target location, as shown in Fig. 8 (d). Due to focusing, the angular spectrum broadens as compared with the flat piston, and, as shown in Fig. 8 (e), the field is no longer homogeneous due to the aberration compensation encoded in the lens. The monitoring hologram is designed to tilt the main directivity lobe $\varphi_h = 11.25°$. When using the lens the steering angle, 11.26°, matches the design value. Finally, the far-field directivity using the hologram is shown in Fig. 8 (f). The beam width is 2.16°, slightly broader than the piston in the far field. Experimental results show also good agreement with the theory for a tilted and focused beam. Note that focusing increases the bandwidth of the angular spectrum and, therefore, focusing on the near field widens the beam width in the far field.

The angular spectrum analysis provides also insights on hologram construction details. By looking in detail at Fig. 8 (e), four bright spots can be seen, marked with arrows. Those spots emerge at directions matching the diffraction grating (DG) angles given by $\sin\varphi = n\lambda/d$, with $n = 1, 2, \ldots$. Note that the squared 500-μm pixels that compose the hologram are slightly larger than the wavelength at 3.5 MHz in water. Therefore, small replicas of the beams are generated at the hologram grid directions, i.e., see directions (u,v) shown in the scheme in Fig. 2 (d). However, since the amplitude on these diffraction grafting lobes is small compared with the main lobe, so is their contribution to the received signal.

3.3. Confocal configuration

Experimental results of stable and inertial mean cavitation doses are presented in Fig. 9. On each graph, both vessel phantoms are shown: the straight tube is represented by a continuous line and the knot phantom by a dashed line. Grey curves stand for baseline (BL) measurements, where only PBS is circulating through the tube, while red curves stand for measurements with circulating microbubbles. Mean cavitation dose for the confocal configuration is measured at 6 different pressures ranging between 178 kPa to 1.54 MPa.

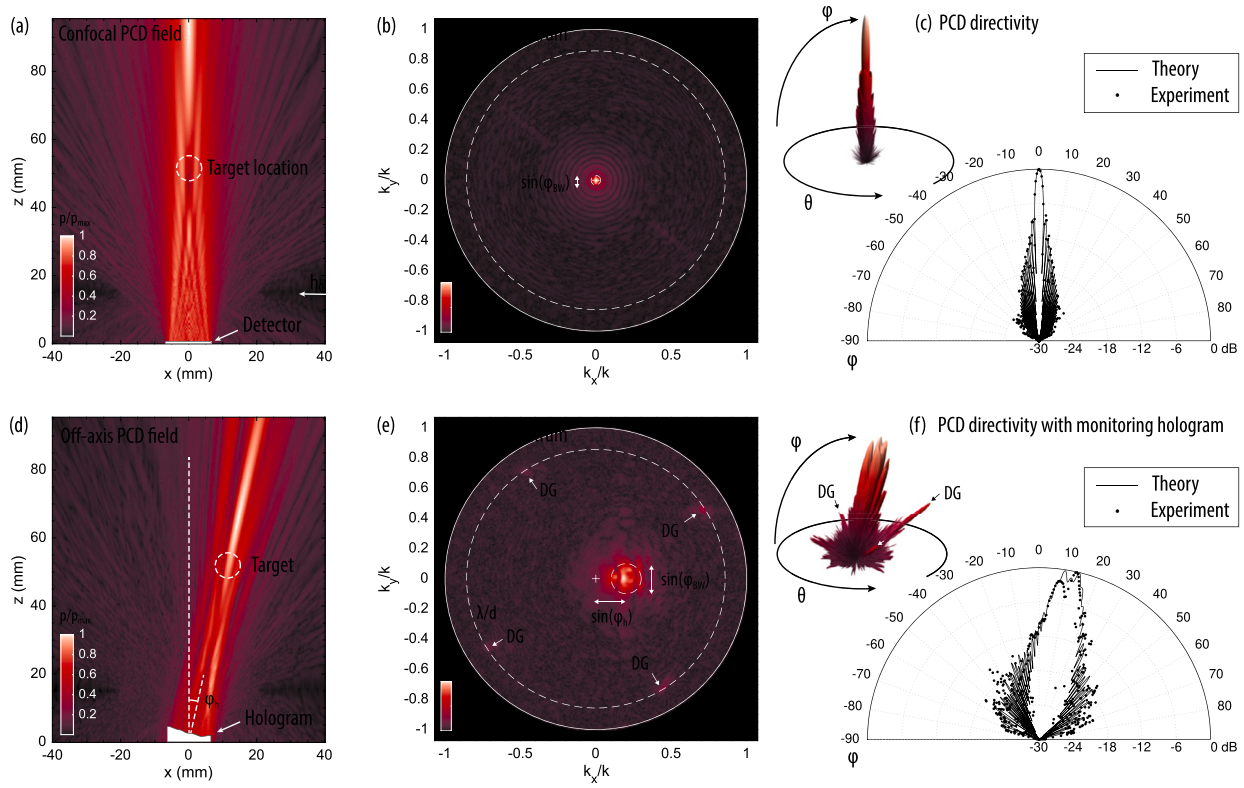


Fig. 8. Passive cavitation detector (PCD) response. (a) Experimental field for the confocal configuration measured in the $p(x,z)$ plane at $y=0$, (b) Corresponding experimental angular spectrum $|p|^2(k_x,k_y)$, showing the normalized angular distribution of the energy for each wavevector component, (c) PCD directivity as a function of the elevation angle. (d) Experimental field including the monitoring hologram for the off-axis configuration, (e) corresponding experimental angular spectrum, (f) PCD directivity including the monitoring lens as a function of the elevation angle.

For all cases, and as expected, mean cavitation dose index grows as pressure increases when microbubbles are circulating. In contrast, baseline slightly increases with moderate pressure amplitudes. At higher pressures, baseline also grows, indicating that nonlinear effects can also be activated in the absence of microbubbles inside of the phantom. By looking at the stable mean cavitation dose based on harmonics, depicted in Fig. 9 (a), we observe that stable cavitation is occurring in the range of pressure 0.4-0.95 MPa. Up to 0.95 MPa, the baseline starts growing and microbubble curves start levelling off. On the other hand, dICD results, Fig. 9 (c), show that at moderate pressure, lower than 0.5 MPa, there is no relevant difference between the baseline and including microbubbles, which indicates that no inertial cavitation is occurring. From 0.66 MPa to the maximum measured pressure (1.53 MPa) dICD baseline remains stable while dICD value for microbubbles increases significantly. Indeed, when stable cavitation occurs, a gain of energy is observed around harmonic components of the received signal spectrum, reflected by the $dSCD_h$ value, but when cavitation becomes inertial, the energy is transferred not only to higher harmonics, but to anharmonic components and, finally, generating broadband noise. This is the reason why $dSCD_h$ tends to stabilize at higher pressure, while, in contrast, dICD increases.

On the other hand, results provided by $dSCD_u$, shown in Fig. 9 (b), follow an intermediate trend. Before reaching high pressure, baseline remains almost constant and $dSCD_u$ is activated for pressures slightly higher than for $dSCD_h$. This latter activation also is a consequence of the harmonic cascade during the nonlinear oscillations of the microbubbles, where even multiples of the fundamental frequency emerge as higher order nonlinear processes. However, $dSCD_u$ values present a low dynamic range (0.01 mV) for this setup. Note that both, $dSCD_h$ and ICD indexes show a much larger dynamic range, ranging from 10 to 40 times greater. Note the limited bandwidth of the PCD does not capture the subharmonic and other low-frequency ultra-harmonic components. Therefore, for further analysis only the $dSCD_h$ and dICD will be analysed.

Finally, it is worth noting here that similar results have been obtained with both vessel phantoms, i.e., the straight tube and the knot vessel phantom, shown as continuous and dashed lines, respectively, in Figs. 9 (a-c). The specific values of both phantoms barely differ, and the pressure-dependent trends for all indexes are similar. However, the physical alignment using the straight tube is much cumbersome than using the knot because of the small size of the former phantom. To minimize the misalignment uncertainty using the monitoring lens for the off-axis configuration, which as shown above exhibits sharper near-field directivity, we will only consider the knot tube.

3.4. Off-axis configurations

The second series of experiments consider the off-axis hologram with and without using the monitoring lens. Here, results of SCD_h and ICD are respectively normalized by the corresponding baseline so that we only see the contribution of microbubbles cavitation. Normalized cavitation dose results are shown in Fig. 10 (a-c), in logarithmic scale for convenience. Note that pressure values take into account system calibration, therefore, while same voltage inputs were used for all measurements, pressure amplitude differs depending on configuration. For confocal configuration (Fig. 10 (a)) maximum pressure value reaches 1.5 MPa whereas for off-axis and holographic monitoring configurations it stops at 1.16 MPa (Figs. 10 (b,c)).

As observed for the confocal configuration, for low pressure levels, mild or no cavitation is detected. As we increase the pressure amplitude, stable cavitation is first generated, and as a consequence we observe an increase of the $\langle dSCD_h \rangle$ value. Then, for higher pressure amplitudes, we observe a stabilization of the $\langle dSCD_h \rangle$ value due to energy transference to ultra-harmonic components. Finally, inertial cavitation is activated

Table 1
Sigmoid model fitting parameters to the normalized stable cavitation dose data, $\langle dSCD_h \rangle$, and the normalized inertial cavitation dose data, $\langle dICD \rangle$.

	$\langle dSCD_h \rangle$					$\langle dICD \rangle$				
	p_{th} (MPa)	β (a.u.)	D_{max} (a.u.)	D_0 (a.u.)	R^2 (a.u.)	p_{th} (MPa)	β (a.u.)	D_{max} (a.u.)	D_0 (a.u.)	R^2 (a.u.)
Confocal configuration	0.54	11.52	1394	4.02	0.996	1.09	8.19	303.7	7.97	0.986
Off-axis configuration	0.36	13.41	62.2	14.18	0.956	9.50	0.64	3940	0.12	0.652
Monitoring lens configuration	0.51	9.09	496.1	4.05	0.933	0.87	9.03	61.42	1.65	0.994

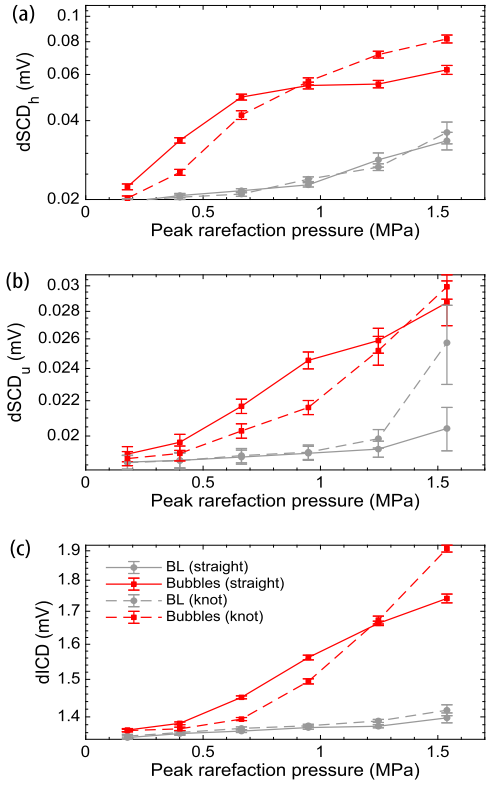


Fig. 9. Mean cavitation doses measured for the confocal configuration. (a) Stable mean cavitation dose based on harmonic contribution ($dSCD_h$), (b) stable mean cavitation dose based on ultraharmonic contribution ($dSCD_u$) and (c) inertial mean cavitation dose based on broadband noise (dICD), measured using microbubbles (red) and PBS only (grey). Both configurations of the vessel phantom are compared, (continuous line) straight vessel phantom and (dashed line) knot vessel phantom.

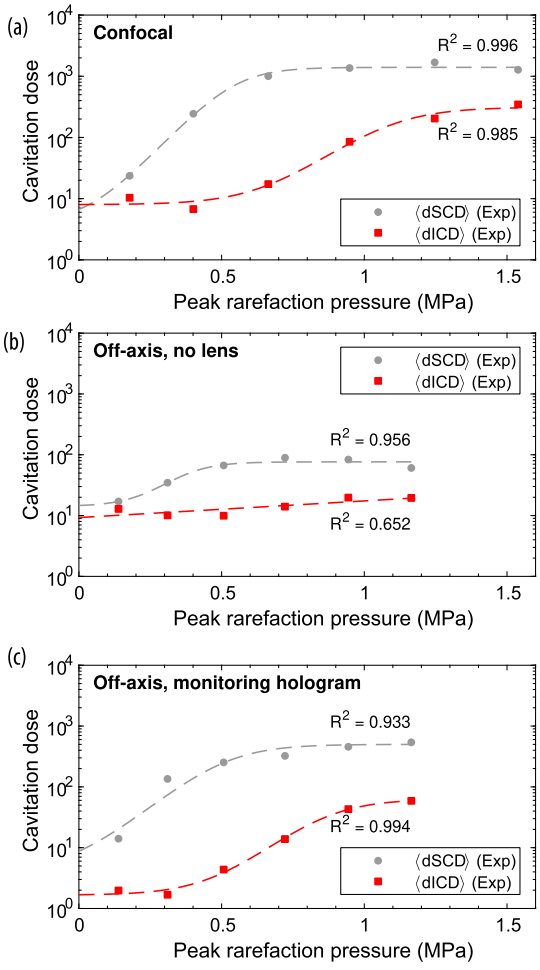


Fig. 10. Experimental results of normalized cavitation doses $\langle dSCD_h \rangle$ (grey markers) and $\langle dICD \rangle$ (red markers), for the knot vessel phantom. (a) Confocal, (b) off-axis and (c) holographic monitoring configurations. A sigmoid model is fitted to experimental data (dashed lines).

and $\langle dICD \rangle$ starts to grow. We propose an empirical sigmoid function, as described in Section 2.6, to model this complex dynamical processes in order to describe the growth and saturation of cavitation dose indexes. The logistic curve given by Eq. (13) is fitted to experimental data, as shown by dashed lines in Figs. 10 (a-c), and the goodness of the fit is given by the indicator R^2 (square of the correlation between the sigmoid function and experimental results). The fitting parameters are listed in Table 1.

For the confocal configuration, we can see in Fig. 10 (a) that the sigmoid model fits well experimental results for stable cavitation. The index $\langle dSCD_h \rangle$ increases until 0.6 MPa, where it reaches a stable state. On the other hand, the sigmoid model fits the experimental $\langle dICD \rangle$ data with a larger margin of error. Note saturation for inertial cavitation was not observed in this pressure amplitude range. However, the initial growth of the $\langle dICD \rangle$ as described by the data can be modelled by the logistic curve.

For the off-axis configuration, the normalized cavitation dose shown in Fig. 10 (b) describes that $\langle dSCD_h \rangle$ saturates with much less dynamic range than for confocal configuration. On the other hand, inertial cavitation is barely detected, i.e., $\langle dICD \rangle$ level is low and does not change with pressure amplitude. Indeed, a lower amplitude is to be expected in reception in this case due to the lateral offset of the focal zone generated by the therapeutic holographic lens, combined with the narrow directivity of the PCD. The R^2 indicator also demonstrates that experimental values are not reliable enough to fit well sigmoid curves, especially in the case of $\langle dICD \rangle$ data for describing inertial cavitation.

In contrast, this situation is reversed when the holographic monitoring lens is used. The cavitation doses shown in Fig. 10 (c) present a similar behaviour than for the original confocal configuration. First, both $\langle dSCD_h \rangle$ and $\langle dICD \rangle$ amplitudes are of a same order of magnitude than for the confocal case. Note the therapeutic beam in this configuration is exactly the same as in the off-axis configuration, and cavitation levels are expected to be similar. However, by manipulating PCD directivity with the 3D-printed monitoring hologram we are able to receive

higher signal level and thus detect microbubbles cavitation. When sigmoid curve is fitted to the experimental $\langle dSCD_h \rangle$ and $\langle dICD \rangle$ data, the dynamics of the cavitation dose are recovered. Moreover, R^2 indicators show a good fitness value between experimental results and fitted model. Note that, when targeting off-axis but using the monitoring lens, the fitting parameters, in particular the pressure threshold (p_{th}) and the transition slope (β), are similar than the ones obtained for the confocal configuration.

4. Discussion

Therapeutic holograms have the ability to steer the focal spot of a source, adapting the size and position of the acoustic image to the therapeutical target, and, in addition, compensating the aberrations produced by the skull bones. This approach results in a low-cost technology that might be used for blood-brain barrier opening. In this way, it may be desirable to use an accordingly low-cost monitoring tool, like cavitation detection, to track the treatment.

To capture cavitation activity, the aperture of passive cavitation detectors for these applications is usually large in order to provide a good sensitivity. This also results in highly directive receivers, and out-of-axis sources are strongly attenuated. Cavitation activity produced out of the axis of these receivers is poorly detected. As demonstrated in this paper, cavitation doses provided by off-axis targets might be biased and/or unreliable. Any small cavitation produced at the axis of the receiving beam will be detected with a much higher amplitude than cavitation signals at the interest location, masking the interest signals. These sensors are suitable for confocal systems, where the therapeutic focal spot is aligned with the detector main lobe. However, the use of standard PCDs to monitor steered holographic devices, where the therapeutic focal spot may be at off-axis, might be limited.

The monitoring holograms proposed in this paper are designed to beamform in reception the signals generated at a target focal spot, inside the skull. The retrieved cavitation doses present the same dynamics as for a confocal configuration, and therefore, might be used to monitor BBB opening treatments produced by therapeutical holograms in a reliable and low-cost way. Note that, although this approach cannot provide spatial information, these lenses are analogous to the reading of cavitation mapping systems at desired spot, i.e., beamforming is passively performed by the engineered lens at the target of interest.

We have observed that the dynamics of mean cavitation dose depending on pressure follows a sigmoid function. For confocal configurations, stable cavitation regime is indicated by moderate and rising level of $\langle dSCD_h \rangle$ while $\langle dICD \rangle$ remains low and stable with pressure amplitude. On the other hand, inertial cavitation regime is characterized by a steady and intense $\langle dSCD_h \rangle$ and moderate and rising $\langle dICD \rangle$. Off-axis configuration on the absence of the monitoring lens causes amplitude loss at reception because of the narrow directivity of the PCD and both, stable and inertial regimes are not clearly identified. However, by using the passive cavitation beamforming strategy applying the monitoring hologram on the PCD, the same cavitation dynamics as for the confocal configuration can be recovered. By measuring cavitation doses, i.e., $\langle dSCD_h \rangle$ and $\langle dICD \rangle$, we can obtain the region between the sigmoids in which moderate stable cavitation is occurring, but inertial cavitation remains low. For this system, this regime is achieved when the peak rarefaction pressure is between 0.3 MPa and 0.6 MPa. These values fit the ones given for a safe and effective BBB opening using a transducer of similar features [15]. One note, regarding safety, recovering accurate in-target inertial cavitation dose is crucial to prevent any sort of vascular damage. Challenges in accurately recovering the inertial cavitation dose, particularly when its position is altered by steering relative to the directional PCD, could contribute to the unforeseen T2* hypo-intensities observed in multiple clinical trials on BBB opening [18,19,14,47].

Note that in this study we mainly take into account harmonic components for stable cavitation because ultra-harmonic cavitation level was weak. This is caused by the frequency range of the PCD. Indeed, central frequency of the focused ultrasound transducer is $f_0 =$ 500 kHz and usually, the lower ultra-harmonics, i.e., the sub-harmonic at 250 kHz and its even multiples, are those with the greatest amplitude. However, the PCD has a central frequency of 3.5 MHz and the lower cut-off frequency (-6 dB) is 1.75 Hz. Reception bandwidth is centred on high-frequency ultra-harmonics which present a low amplitude. Therefore, $dSCD_u$ in this study did not provide clear insight into the cavitation dynamics at the focal spot.

A possible modification of the system might be to use a defocusing hologram or lens for wide angle covering. In this way, maintaining the high sensitivity or a large-aperture PCD, cavitation activity emerging from any location may be detected. However, note this kind of configurations are less specific to monitor the activity at the target. Such configuration may provide cavitation signals from other regions. Indeed, the proposed holograms are designed to beamform cavitation activity generated at the target, and are suitable to monitor the cavitation activity locally. In this study, a simple vessel phantom was used in order to generate cavitation only at the focal spot, and cavitation signals were detected accordingly. In contrast, in a in-vivo scenario, capillaries and blood vessels are present all over the brain and cavitation signals of different level may be generated at any location. Passive beamforming using holograms will amplify signals at the target location, ensuring the cavitation dose corresponds with this location. In addition, note that holograms provide strong flexibility to produce multi-focal therapeutic beams or wide focal spots. In the same way, monitoring holograms may also be designed to provide a directivity pattern with several lobes for the detector, each one matching the size and location of a therapeutical focal spot. Finally, note that in this work the monitoring lens was 3D-printed separately to the therapeutic hologram, but in a relevant scenario both lenses can be manufactured simultaneously in the same piece to ensuring robustness under misalignment.

In addition, it should be noted here that since the lens is 3D printed in a solid material, its focus is fixed and, in principle, no major changes can be made to the location of the focal point. However, holograms do allow for a certain degree of steering, e.g., the system can be mechanically moved up to tens of millimetres, enough to cover a larger area [48]. By reciprocity, passive cavitation beamforming will benefit from this effect and the whole system might move together to target and monitor various locations. An alternative to mechanical movements is to produce a larger volumetric focal spot [49], and adapt this focal spots to the whole therapeutic target. In this way, the sensitivity of a PCD could be adjusted to monitor cavitation at a wider focal area, avoiding the need to mechanically move the entire system. It should be noted that these approaches are limited to a specific target and patient. For a different individual, a new therapeutic and monitoring hologram must be designed and 3D printed because skull aberrations differ between patients [22]. To go beyond fixed 3D-printed holograms, using reconfigurable holograms [50] in reception might be able to change the location of the focal spot of cavitation monitoring in real time.

5. Conclusions

In this work, we have presented a simple but low-cost method to beamform the cavitation signals produced at the focus of a therapeutical ultrasound system to locally monitor the cavitation activity. The method is based on 3D-printed holograms, where a lens is designed to encode the temporal delays of the beamformer, aligning the cavitation emission of the microbubbles at the target focal spot.

We have tested the concept using a setup where both therapeutic and monitoring systems are based on 3D-printed acoustic holograms. The first hologram was used for the therapeutic system to focus the ultrasound beam at a target within a macaque skull, matching the location of the post-commissural putamen, which is located off-axis. Then, a monitoring lens is designed to steer the directivity of the PCD at the location of the therapeutic target and, in addition, compensating the skull

aberrations. In this way, this monitoring hologram encodes a passive beamformer that aligns the cavitation signals generated at the target. Retrieved cavitation doses indicate that these monitoring lenses allow to locally monitor the cavitation activity.

This approach might be of interest for therapeutic ultrasound systems whose focal spot is not aligned with the detector, like systems using acoustic holograms or phased arrays systems when large electronic steering is applied, and for transcranial focused ultrasound applications such as BBB opening or any other cavitation-based therapy, where treatments can be monitored using a spectral analysis of the cavitation signals captured by a single-channel passive cavitation detector. In this way, passive cavitation beamforming can be used to estimate off-axis cavitation doses and to locally monitor the cavitation activity of microbubbles, thus opening a new path to low-cost monitoring of therapeutic ultrasound systems.

CRediT authorship contribution statement

Nathalie Lamothe: Writing – review & editing, Writing – original draft, Visualization, Validation, Software, Resources, Methodology, Investigation, Data curation. **Diana Andrés:** Writing – review & editing, Validation, Software, Methodology, Investigation, Formal analysis, Data curation. **Alicia Carrión:** Writing – review & editing, Validation, Software, Resources, Methodology, Investigation, Funding acquisition, Formal analysis, Conceptualization. **Francisco Camarena:** Supervision, Project administration, Funding acquisition. **José A. Pineda-Pardo:** Formal analysis, Investigation, Resources, Supervision, Validation, Writing – review & editing. **Noé Jiménez:** Writing – review & editing, Visualization, Validation, Supervision, Software, Resources, Project administration, Methodology, Investigation, Funding acquisition, Formal analysis, Data curation, Conceptualization.

Declaration of competing interest

The authors declare the following financial interests/personal relationships which may be considered as potential competing interests: Noé Jiménez reports financial support was provided by Spain Ministry of Science and Innovation grant RYC2021-034920-I. Diana Andrés reports financial support was provided by Government of Spain Ministry of Universities grant FPU19/00601. Noé Jiménez reports financial support was provided by Agencia Estatal de Investigación grants PID2022-142719OB-C21, CNS2023-145707. Noé Jiménez reports financial support was provided by Agència Valenciana de la Innovació grants INNVA2/2022/11 and INNEST/2022/345. Noé Jiménez reports financial support was provided by Generalitat Valenciana grants EDGJID/2021/189, CIGE/2021/175, CIAICO/2023/052 and FDEGENT/2019/004. If there are other authors, they declare that they have no known competing financial interests or personal relationships that could have appeared to influence the work reported in this paper.

Data availability

Data will be made available on request.

Acknowledgements

This research has been supported by the Ministerio Español de Ciencia e Innovación and the Ministerio de Universidades grants FJC2019-040453-I, RYC2021-034920-I, FPU19/00601 and Agencia Estatal de Investigación grants PID2022-142719OB-C21 and CNS2023-145707 funded by MCIN/AEI/10.13039/501100011033; Agència Valenciana de la Innovació grants INNVA2/2022/11 and INNEST/2022/345; Generalitat Valenciana grants EDGJID/2021/189, CIGE/2021/175, CIAICO/2023/052, CIPROM/2021/003, FDEGENT/2019/004 and IDIFEDER/2021/004.

We acknowledge Jose Luis Alonso for technical support in the design of the experimental setup.

Appendix A. Sensitivity analysis

The limitations on lens construction and the uncertainty of physical parameters can impact on the acoustic performance of the system. For instance, the proposed lens for monitoring was designed using a pixel width of $\Delta x = 500$ μm. In addition, the printing layer thickness in the z-direction was set to $\Delta z = 50$ μm. Note the particular printer used in this work can resolve up to $\Delta x = 10$ μm and $\Delta z = 25$ μm. While these values are much smaller than the wavelength of the therapeutical beam at 500 kHz ($\lambda = 3$ mm, $\lambda/\Delta x = 6$ and $\lambda/\Delta z = 60$), for the monitoring lens at 3.5 MHz these parameters are more similar to the wavelength ($\lambda = 3$ mm, $\lambda/\Delta x = 0.86$ and $\lambda/\Delta z = 8.6$). The pixel width is of the order of the wavelength and, therefore, diffraction grating lobes can appear, as shown in this work. On the other hand, the axial dimension is quantized in 8.6 steps per wavelength, which means that the lens

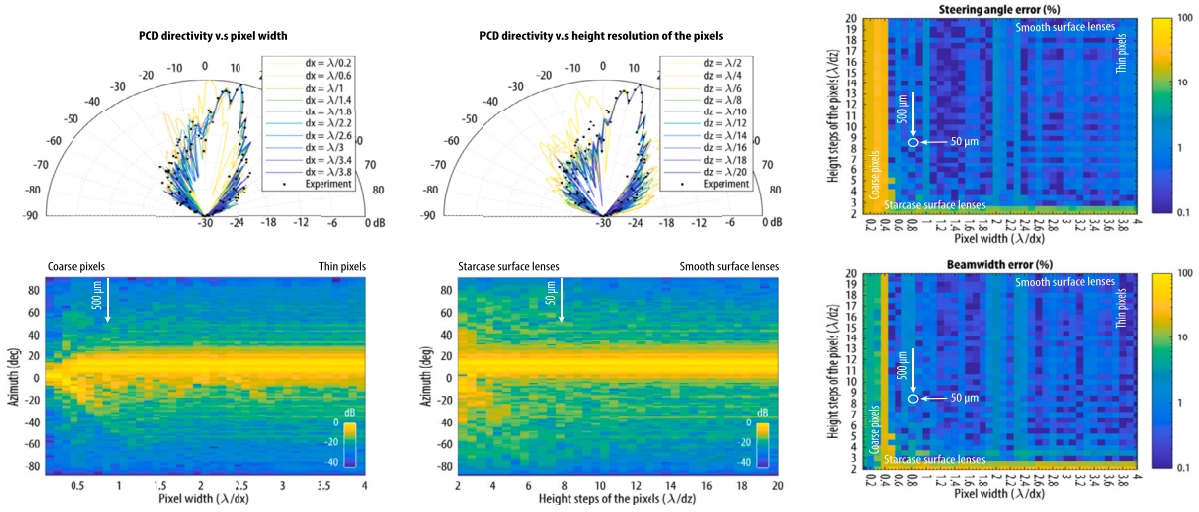


Fig. A. 11. Results of the sensitivity analysis. (a) Directivity curves sweeping the pixel size (dx) for a layer of $\Delta z = \lambda/20$. (b) Directivity curves sweeping the number of steps in the axial direction (dz) for a pixel width of $\Delta x = \lambda/4$. (c) Full directivity data as a function of dx for $\Delta z = \lambda/20$. (d) Full directivity data as a function of dz for $\Delta x = \lambda/4$. (e) Relative error of the steering angle as a function of the geometrical parameters. (f) Relative error of the PCD beam-width as a function of the geometrical parameters.

can only synthesize at a finite number of phase values. To test the impact of these geometrical constraints on the performance of the lens, a set of 1480 simulations were performed by sweeping the geometrical parameters. The lateral size of the pixels was varied in the range $0.1 < \lambda/\Delta x < 4$ (4.3 mm > Δx > 107 μm), and the height of the printing layer was modified in the range $2 < \lambda/\Delta z < 20$ (214 μm > Δz > 21 μm). The PCD directivity was calculated as a function of the receiving angle. From this data, the main receiving angle and the beam-width were calculated. The relative errors between these metrics and the design receiving angle and the beam-width obtained by the theoretical approach were calculated. The results are shown in Fig. 11. It can be observed that when thin pixels are used (large $\lambda/\Delta x$), and when the surface of the lens is smooth by using a small Δz (large $\lambda/\Delta z$) the PCD performs very similar than the expected by the design and, therefore, the errors for the beam parameters are small ($\epsilon < 1\%$). However, when the geometrical parameters are coarse (small $\lambda/\Delta x$ and $\lambda/\Delta z$ ratios), the lens does not perform as expected and PCD directivity does not agree the design, resulting in large and undesirable errors. For the geometric parameters used in this work (annotated in Figs. 11 (c-f)), the beam agrees with the design and we observe small relative errors for both, the tilt angle (around 0.1%) and the beam-width (around 1%). Note that a large variation of these values is observed in the study but, for this simple lens, the errors only become larger than 10% for very coarse grids ($\Delta x > 2\lambda$ and $\Delta z > \lambda/3$).

References

[1] Taylor EM. The impact of efflux transporters in the brain on the development of drugs for cns disorders. Clin Pharmacokinet 2002;41:81–92.

[2] Zhao Z, Nelson AR, Betsholtz C, Zlokovic BV. Establishment and dysfunction of the blood-brain barrier. Cell 2015;163(5):1064–78.

[3] Leinenga G, Langton C, Nisbet R, Götz J. Ultrasound treatment of neurological diseases—current and emerging applications. Nat Rev Neurol 2016;12(3):161–74.

[4] Hsu P-H, Lin Y-T, Chung Y-H, Lin K-J, Yang L-Y, Yen T-C, et al. Focused ultrasound-induced blood-brain barrier opening enhances gsk-3 inhibitor delivery for amyloid-beta plaque reduction. Sci Rep 2018;8(1):12882.

[5] Weber-Adrian D, Kofoed RH, Chan JWY, Silburt J, Noroozian Z, Kügler S, et al. Strategy to enhance transgene expression in proximity of amyloid plaques in a mouse model of Alzheimer's disease. Theranostics 2019;9(26):8127.

[6] Janowicz PW, Leinenga G, Götz J, Nisbet RM. Ultrasound-mediated blood-brain barrier opening enhances delivery of therapeutically relevant formats of a tau-specific antibody. Sci Rep 2019;9(1):9255.

[7] Xhima K, Nabbouh F, Hynynen K, Aubert I, Tandon A. Noninvasive delivery of an α-synuclein gene silencing vector with magnetic resonance–guided focused ultrasound. Mov Disord 2018;33(10):1567–79.

[8] Fan C-H, Ting C-Y, Lin C-Y, Chan H-L, Chang Y-C, Chen Y-Y, et al. Noninvasive, targeted and non-viral ultrasound-mediated gdnf-plasmid delivery for treatment of Parkinson?s disease. Sci Rep 2016;6(1):19579.

[9] Karakatsani ME, Wang S, Samiotaki G, Kugelman T, Olumolade OO, Acosta C, et al. Amelioration of the nigrostriatal pathway facilitated by ultrasound-mediated neurotrophic delivery in early Parkinson's disease. J Control Release 2019;303:289–301.

[10] Bunevicius A, McDannold NJ, Golby AJ. Focused ultrasound strategies for brain tumor therapy. Oper Neurosurg 2020;19(1):9.

[11] Meng Y, Reilly RM, Pezo RC, Trudeau M, Sahgal A, Singnurkar A, et al. Mr-guided focused ultrasound enhances delivery of trastuzumab to her2-positive brain metastases. Sci Transl Med 2021;13(615):eabj4011.

[12] Park SH, Baik K, Jeon S, Chang WS, Ye BS, Chang JW. Extensive frontal focused ultrasound mediated blood–brain barrier opening for the treatment of Alzheimer's disease: a proof-of-concept study. Transl Neurodegener 2021;10(1):1–11.

[13] D'Haese P-F, Ranjan M, Song A, Haut MW, Carpenter J, Dieb G, et al. β-amyloid plaque reduction in the hippocampus after focused ultrasound-induced blood–brain barrier opening in Alzheimer's disease. Front Human Neurosci 2020:422.

[14] Gasca-Salas C, Fernández-Rodríguez B, Pineda-Pardo JA, Rodríguez-Rojas R, Obeso I, Hernández-Fernández F, et al. Blood-brain barrier opening with focused ultrasound in Parkinson's disease dementia. Nat Commun 2021;12(1):779.

[15] Pouliopoulos AN, Wu S-Y, Burgess MT, Karakatsani ME, Kamimura HA, Konofagou EE. A clinical system for non-invasive blood–brain barrier opening using a neuronavigation-guided single-element focused ultrasound transducer. Ultrasound Med Biol 2020;46(1):73–89.

[16] Horodyckid C, Canney M, Vignot A, Boisgard R, Drier A, Huberfeld G, et al. Safe long-term repeated disruption of the blood-brain barrier using an implantable ultrasound device: a multiparametric study in a primate model. J Neurosurg 2017;126(4):1351–61.

[17] Idbaih A, Canney M, Belin L, Desseaux C, Vignot A, Bouchoux G, et al. Safety and feasibility of repeated and transient blood–brain barrier disruption by pulsed ultrasound in patients with recurrent glioblastoma. Clin Cancer Res 2019;25(13):3793–801.

[18] Lipsman N, Meng Y, Bethune AJ, Huang Y, Lam B, Masellis M, et al. Blood–brain barrier opening in Alzheimer's disease using mr-guided focused ultrasound. Nat Commun 2018;9(1):2336.

[19] Abrahao A, Meng Y, Llinas M, Huang Y, Hamani C, Mainprize T, et al. First-in-human trial of blood–brain barrier opening in amyotrophic lateral sclerosis using mr-guided focused ultrasound. Nat Commun 2019;10(1):4373.

[20] Maimbourg G, Houdouin A, Deffieux T, Tanter M, Aubry J-F. 3d-printed adaptive acoustic lens as a disruptive technology for transcranial ultrasound therapy using single-element transducers. Phys Med Biol 2018;63(2):025026.

[21] Jiménez-Gambín S, Jiménez N, Benlloch JM, Camarena F. Holograms to focus arbitrary ultrasonic fields through the skull. Phys Rev Appl 2019;12(1):014016.

[22] Andrés D, Jiménez N, Benlloch JM, Camarena F. Numerical study of acoustic holograms for deep-brain targeting through the temporal bone window. Ultrasound Med Biol 2022;48(5):872–86.

[23] Jiménez-Gambín S, Jiménez N, Camarena F. Transcranial focusing of ultrasonic vortices by acoustic holograms. Phys Rev Appl 2020;14(5):054070.

[24] Kim J, Kasoji S, Durham PG, Dayton PA. Acoustic holograms for directing arbitrary cavitation patterns. Appl Phys Lett 2021;118(5).

[25] Ma Z, Holle AW, Melde K, Qiu T, Poeppel K, Kadiri VM, et al. Acoustic holographic cell patterning in a biocompatible hydrogel. Adv Mater 2020;32(4):1904181.

[26] Andrés D, Vappou J, Jiménez N, Camarena F. Thermal holographic patterns for ultrasound hyperthermia. Appl Phys Lett 2022;120(8).

[27] Andrés D, Rivens I, Mouratidis P, Jiménez N, Camarena F, Ter Haar G. Holographic focused ultrasound hyperthermia system for uniform simultaneous thermal exposure of multiple tumor spheroids. Cancers 2023;15(9):2540.

[28] Jiménez-Gambín S, Jiménez N, Pouliopoulos AN, Benlloch JM, Konofagou EE, Camarena F. Acoustic holograms for bilateral blood-brain barrier opening in a mouse model. IEEE Trans Biomed Eng 2021;69(4):1359–68.

[29] He J, Zhu Y, Wu C, Wu J, Chen Y, Yuan M, et al. Simultaneous multi-target ultrasound neuromodulation in freely-moving mice based on a single-element ultrasound transducer. J Neural Eng 2023;20(1):016021.

[30] McDannold N, Vykhodtseva N, Hynynen K. Targeted disruption of the blood–brain barrier with focused ultrasound: association with cavitation activity. Phys Med Biol 2006;51(4):793.

[31] Tung Y-S, Vlachos F, Feshitan JA, Borden MA, Konofagou EE. The mechanism of interaction between focused ultrasound and microbubbles in blood-brain barrier opening in mice. J Acoust Soc Am 2011;130(5):3059–67.

[32] Arvanitis CD, Livingstone MS, Vykhodtseva N, McDannold N. Controlled ultrasound-induced blood-brain barrier disruption using passive acoustic emissions monitoring. PLoS ONE 2012.

[33] Sun T, Samiotaki G, Wang S, Acosta C, Chen CC, Konofagou EE. Acoustic cavitation-based monitoring of the reversibility and permeability of ultrasound-induced blood-brain barrier opening. Phys Med Biol 2015;60(23):9079.

[34] Tsai C-H, Zhang J-W, Liao Y-Y, Liu H-L. Real-time monitoring of focused ultrasound blood-brain barrier opening via subharmonic acoustic emission detection: implementation of confocal dual-frequency piezoelectric transducers. Phys Med Biol 2016;61(7):2926.

[35] Baseri B, Choi JJ, Tung Y-S, Konofagou EE. Multi-modality safety assessment of blood-brain barrier opening using focused ultrasound and definity microbubbles: a short-term study. Ultrasound Med Biol 2010;36(9):1445–59.

[36] O'Reilly MA, Hynynen K. Blood-brain barrier: real-time feedback-controlled focused ultrasound disruption by using an acoustic emissions–based controller. Radiology 2012;263(1):96–106.

[37] Kamimura HA, Flament J, Valette J, Cafarelli A, Aron Badin R, Hantraye P, et al. Feedback control of microbubble cavitation for ultrasound-mediated blood–brain barrier disruption in non-human primates under magnetic resonance guidance. J Cereb Blood Flow Metab 2019;39(7):1191–203.

[38] McDannold N, Zhang Y, Supko JG, Power C, Sun T, Peng C, et al. Acoustic feedback enables safe and reliable carboplatin delivery across the blood-brain barrier with a clinical focused ultrasound system and improves survival in a rat glioma model. Theranostics 2019;9(21):6284.

[39] Gyongy M, Coussios CC. Passive spatial mapping of inertial cavitation during hifu exposure. IEEE Trans Biomed Eng 2009;57(1):48–56.

[40] Choi JJ, Carlisle RC, Coviello C, Seymour L, Coussios C-C. Non-invasive and real-time passive acoustic mapping of ultrasound-mediated drug delivery. Phys Med Biol 2014;59(17):4861.

[41] Arvanitis CD, Clement GT, McDannold N. Transcranial assessment and visualization of acoustic cavitation: modeling and experimental validation. IEEE Trans Med Imaging 2014;34(6):1270–81.

[42] Jones RM, O'Reilly MA, Hynynen K. Experimental demonstration of passive acoustic imaging in the human skull cavity using ct-based aberration corrections. Med Phys 2015;42(7):4385–400.

[43] Burgess M, Apostolakis I, Konofagou E. Power cavitation-guided blood-brain barrier opening with focused ultrasound and microbubbles. Phys Med Biol 2018;63(6):065009.

[44] Andrés D, Carrión A, Camarena F, Jiménez N. Methods to design and evaluate transcranial ultrasonic lenses using acoustic holography. Phys Rev Appl 2023;20:044071.
[45] Herráez MA, Burton DR, Lalor MJ, Gdeisat MA. Fast two-dimensional phase-unwrapping algorithm based on sorting by reliability following a noncontinuous path. Appl Opt 2002;41(35):7437–44.
[46] Treeby BE, Jaros J, Rendell AP, Cox B. Modeling nonlinear ultrasound propagation in heterogeneous media with power law absorption using ak-space pseudospectral method. J Acoust Soc Am 2012;131(6):4324–36.
[47] Pineda-Pardo JA, Gasca-Salas C, Fernández-Rodríguez B, Rodríguez-Rojas R, Del Alamo M, Obeso I, et al. Striatal blood–brain barrier opening in Parkinson's disease dementia: a pilot exploratory study. Mov Disord 2022;37(10):2057–65.
[48] Maimbourg G, Houdouin A, Deffieux T, Tanter M, Aubry J-F. Steering capabilities of an acoustic lens for transcranial therapy: numerical and experimental studies. IEEE Trans Biomed Eng 2019;67(1):27–37.
[49] Melde K, Kremer H, Shi M, Seneca S, Frey C, Platzman I, et al. Compact holographic sound fields enable rapid one-step assembly of matter in 3d. Sci Adv 2023;9(6):eadf6182.
[50] Ma Z, Melde K, Athanassiadis AG, Schau M, Richter H, Qiu T, et al. Spatial ultrasound modulation by digitally controlling microbubble arrays. Nat Commun 2020;11(1):4537.